Available online at www.sciencedirect.com
ScienceDirect
Materials Chemistry and Physics 109 (2008) 61–76
MATERIALS CHEMISTRY AND PHYSICS
www.elsevier.com/locate/matchemphys

# Nd:YAG laser welding of aerospace grade ZE41A magnesium alloy: Modeling and experimental investigations

H. Al-Kazzaz [a], M. Medraj [a,*], X. Cao [b], M. Jahazi [b]

[a] *Department of Mechanical Engineering, Concordia University, Montreal, Canada*
[b] *Aerospace Manufacturing Technology Centre, Institute for Aerospace Research, National Research Council Canada, Montreal, Canada*

Received 2 July 2007; received in revised form 25 October 2007; accepted 31 October 2007

**Abstract**

Keyhole formation as well as the geometry of weld profiles during Nd:YAG laser welding of ZE41A-T5 were studied through combining various models and concepts. The results indicated that weld width and fusion area decrease with increasing welding speed. In the case of partially penetrated welding, penetration depth decreases with increasing welding speed. Also, the model predicted that excessive decrease in laser power or increase in defocusing distance decreases surface power density, thereby changing the welding mode from fully penetrated keyhole, to partially penetrated keyhole, and then to the conduction mode. The predicted conditions for keyhole stability and welding modes as well as the weld profiles for various processing conditions were validated by some selected welding experiments. These experiments included studying the effects of welding speed, laser power, joint gap and laser defocusing on the weld geometry of 2- and 6-mm butt joints or bead-on-plates of ZE41A-T5 sand castings using a continuous wave 4 kW Nd:YAG laser system and 1.6-mm EZ33A-T5 filler wire. Good agreements were found between the model predictions and experimental results indicating the validity of the assumptions made for the development of the model.


*Keywords:* Laser welding; Modeling; Mg sand casting; Filler wire; Keyhole mode

## 1. Introduction

Laser welding is in general a keyhole-mode fusion welding technique that provides line-heating source through the material thickness [1,2]. Compared with conventional fusion welding processes, laser welding produces higher penetration depth in a single pass [2]. The keyhole can be described as a vapor capillary tube surrounded by a molten metal [3] and is formed when the laser power absorbed by the metal is greater than the material specific intensity threshold [3,4]. This means that the critical intensity limit for keyhole formation must be overcome by the intensity of the laser beam. The presence of such conditions results in the creation of a moving keyhole surrounded by a molten metal due to the absorption of incident laser beam [5]. Because of the high welding speed [3], the molten metal is rapidly solidified behind the moving keyhole creating the joint between the welding parts (Fig. 1). The heating power is obtained by focusing the laser beam into a very small spot that provides a very high power density [2,3,5,6]. The range of power density that creates the keyhole is from $10^3$ to $10^5$ W mm$^{-2}$, and above this range cutting and drilling are usually achieved [2].

The stability of the keyhole depends on the force balance between the keyhole wall and the molten metal around it, and this can be described by the following equation [5]:

$$P_v = P_\sigma \tag{1}$$

Where $P_v$ is vaporization pressure, and $P_\sigma$ surface tension.

This means that the stability of the keyhole depends on the force balance between the vapor pressure and the surface tension pressure. The vapor pressure tends to open the keyhole whereas the surface tension pressure tends to close it. The above findings have been confirmed by Zhao and co-workers [4,7] and Punkari et al. [8]. If the laser intensity overcomes the threshold intensity of the material, the keyhole forms and induces two main absorption mechanisms; Fresnel and plasma absorption. The Fresnel absorption can be divided into the first Fresnel absorption and multiple reflections. The first Fresnel absorption represents the first absorption occurring due to the first interaction of the laser ray with keyhole wall. The temperature inside the keyhole will be much higher than the evaporation temperature at the key-

* Corresponding author. Tel.: +1 514 848 2424x3146; fax: +1 514 848 3175.
*E-mail address:* mmedraj@encs.concordia.ca (M. Medraj).

0254-0584/$ – see front matter © 2007 Elsevier B.V. All rights reserved.
doi:10.1016/j.matchemphys.2007.10.039

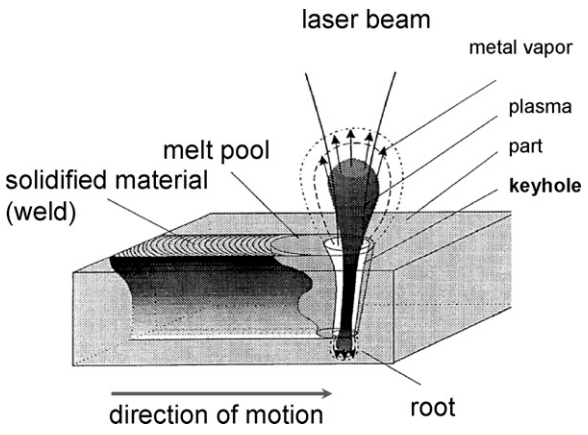


Fig. 1. Laser welding in the keyhole mode.

hole wall which leads to the formation of ionized gases which absorb energy from the reflected laser rays. The energy balance between these effects and the heat loss through the keyhole wall will determine the keyhole profile.

A useful method to describe the keyhole profile in a plane parallel to welding direction for the front and rear walls during $CO_2$ laser welding of steel was proposed by Kaplan [9]. A conical shape was assumed for the keyhole for the purpose of calculating the multiple reflections of the laser ray. Also, only normal incidence absorption (ray perpendicular to the keyhole wall) during multiple reflections was considered in the calculations. The plasma absorption was estimated using the value of the intensity that is left after undergoing multiple reflections and by defining the mean path of the rays as one and half times the depth of a blind keyhole. The intensities obtained for multiple reflections and plasma were both assumed to be for the same layer at the first Fresnel absorption (the first interaction of the laser ray with the keyhole wall). Lampa et al. [10] modeled the weld pool geometry generated during $CO_2$ blind laser welding of steel by applying Kaplan's [9] method. They calculated the top weld width and assumed the bottom weld width to be half of the top weld width for blind keyhole-mode welding based on the experimental observations. To account for the effect of thermocapillary (Marangoni) flow, Lampa et al. [10] assumed that the thermal conductivity on the top is 2.5 times the real thermal conductivity, and they corrected the source strength on the top of the keyhole accordingly. The penetration depth was calculated by dividing the total power absorbed by the keyhole by the average line source strength, using the artificial thermal conductivity value at the top, and the real thermal conductivity value at the bottom.

The Fresnel absorption and reflection in the keyhole were studied by Jin et al. [11]. Glass was used to capture the keyhole profile in a plane parallel to the welding direction, and the multiple reflections and the laser absorption inside the asymmetric keyhole were analyzed using geometrical optics theory. The plasma absorption was avoided in the above study since the glass GG17 used had very high ionization energy and thus plasma is difficult to form. On the other hand, Solana and Negro [12] studied the effect of multiple reflection and plasma on the blind keyhole profile. They developed a numerical model with an initial keyhole having conical shape based on assumed keyhole top radius and penetration depth. It was found that the keyhole profile varies with the Fresnel and plasma absorption values; however, the energy conservation at the keyhole wall was not considered.

In the present work, Kaplan's [9] and Lampa et al.'s [10] models were modified and combined with the calculation methods of the multiple reflection [11] and plasma absorption [12] to calculate the weld geometry profiles. Although the keyhole in the actual process is asymmetric in the plane parallel to welding direction, it is symmetric in the plane perpendicular to welding direction. In addition, the perpendicular plane also reveals the weld geometry profile, and thus it was used in the calculations of this study. This was achieved by calculating the energy balance at each layer of the keyhole and by registering the location of each multiple reflection and plasma absorption in the corresponding layer. A correction factor was used, instead of artificial thermal conductivity values, to estimate the effect of the widening of the weld width due to the thermocapillary flow. This factor was used to correct the source strengths based on the experimental investigation during laser welding of Mg alloy. Finally, the modeling results were verified by experiments.

## 2. Experimental procedures and materials

### 2.1. Materials and equipment

The experimental material was aerospace grade sand cast ZE41A-T5 (Mg–4.2Zn–1.2Ce–0.7Zr) magnesium alloy. The cast plates had sizes of approximately 300 mm × 150 mm × 3–7 mm. The plates were cut into four small pieces for laser welding, each with approximate sizes of 150 mm × 75 mm × 3–7 mm. The magnesium castings were then machined to 2 and 6 mm thicknesses. The joint faces were also machined along the length for all the specimens. Prior to laser welding the joint faces and their surroundings were carefully cleaned by acetone to remove any contaminations.

The laser welding machine used in this study is a continuous wave (CW) 4 kW HL4006 Nd:YAG (neodymium-doped yttrium aluminum garnet) laser system equipped with an ABB robotic and magnetic fixture system. A focal length of 150 mm and a fiber diameter of 0.6 mm were employed. Helium was used to shield the top surface and argon for the bottom surface of the workpieces as shown in Fig. 2. The flow rates were 18.9 and 21.21 $min^{-1}$ (40 and 45 $ft^3\,h^{-1}$) for the top and bottom surfaces, respectively. The shielding gas, He, was directed to the top surface of the workpiece at an angle of 30° (with the horizontal) and Ar was vertically and uniformly directed to the bottom surface. The workpieces (butt joint) were positioned and clamped in a fixture with various gap size from 0 to 0.6 mm. Defocusing range was between 0 and −4 mm with 0.45 mm focal spot diameter.

A filler wire of EZ33A-T5 (Mg–3Re–2.5Zn–0.6Zr) Mg alloy with 1.6 mm diameter and 990 mm length was used through a wire feeding mechanism. Laser welding using filler wire is getting more attention since it might solve many of the problems facing autogenous welding. The most important advantages of using filler material include improving weld properties, increasing the gap between the welding parts, and welding thick sections using a multi-pass technique. Compared with other welding techniques laser welding requires less filler wire per meter of welded seam, underfill and notching effect can be overcome using filler wire, and finally the porosity of the welded joint can be reduced using filler metal [2,3]. The filler wire was positioned at the intersection of laser beam and top surface of the workpiece. A delivering angle of 60° was used between the filler and the laser beam axis to reduce the contact area between them. During laser welding, the workpieces were stationary while the laser beam scanned at a power value between 2.5 and 4 kW and a speed from 2 to

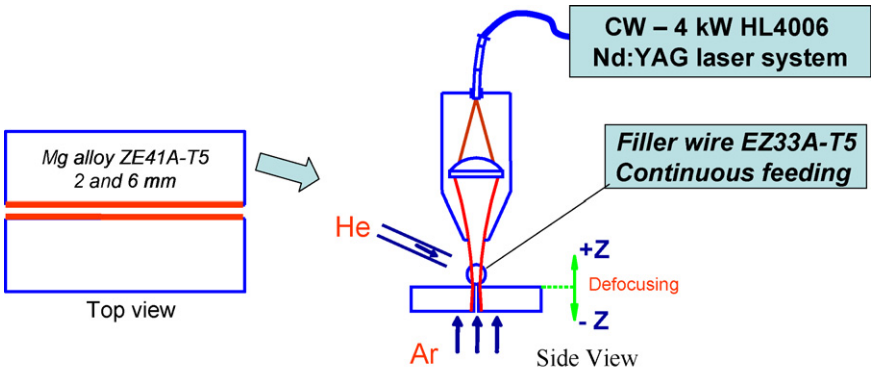


Fig. 2. Experimental setup for laser welding of Mg alloy using continuous feeding mechanism connected with the laser head.

7 m min$^{-1}$. Wire feeding rate was calculated using volume flow rate constancy:

$$\text{Wire feed rate} = \frac{\text{welding speed} \times \text{gap area}}{\text{filler wire area}} \quad (2)$$

After welding, a length of approximately 20–30 mm was cut from both ends of each joint to exclude the unstable segments appearing at the start and end of laser welding. Cross-sectional samples for metallurgical examination were cut from the weld joints at three locations (start, middle and end). The polished samples were then etched in Nital solution (1 ml volume of $HNO_3$ in 100 ml ethanol). The dimensions of the fusion zone (FZ) were measured using an Olympus optical microscope equipped with Discover Essential image analyzer software. The average values were calculated from the quantitative measurements of the three specimens (start, middle and end).

### 2.2. Key experiments used for model verification and comparison

Butt joints with 2 and 6 mm thickness, and bead-on-plate welding with 6-mm thickness were used to verify the modeled fusion zone geometries. The samples were divided into groups as shown in Table 1.

## 3. Calculations of laser efficiencies from the experimental FZ geometries

In a previous study [13], it was found that the use of filler wire had no significant effect on the FZ area if the wire feed rate used was calculated from equation 2. In this modeling study, the process of welding using filler wire will be simplified to the autogenous condition. However, the increase in laser power losses must be compensated for this setup. For this purpose, laser welding process was specially performed for two joints: one welded autogenously (sample 29) and one using filler wire (sample 30), while the other process parameters (i.e. laser power, welding speed, thickness, focusing parameters) were kept the same as summarized in Table 1.

### 3.1. Laser process efficiency

In keyhole-mode laser welding process, the beam passes through multiple stages till it is converted to effective power that melts the base metal (BM) and produces the weld seam as shown in Fig. 3. The keyhole will be created after overcoming the threshold intensity ($I_s$) which is determined by material's vaporization temperature ($T_v$), thermal conductivity ($k$) and absorptivity at normal incidence ($A$) [14]:

$$I_s \propto \frac{T_v k}{A} \quad (3)$$

Before the laser beam enters the keyhole, part of the laser power ($P$) will be lost due to reflection ($P_{ref}$) and the absorption by plasma plume ($P_{plume}$) [10]:

$$P_{\text{entering the keyhole}} = P - P_{ref} - P_{plume} \quad (4)$$

Before the laser ray reaches the keyhole wall, part of the ray will be absorbed by the plasma that exists inside the keyhole. Once the laser ray reaches the keyhole wall, it is partially absorbed (first Fresnel absorption). The percentage absorbed depends on the wall angle and material's physical properties. The reflected intensity will pass through multiple reflections inside the keyhole. Between each reflection the laser ray will lose some of its intensity due to plasma absorption. The laser ray finally leaves the keyhole from the top in the case of blind keyholes, or from both the bottom and the top for open keyholes.

The coupling efficiency ($\eta_A$) is defined as the portion of the laser power available to the workpiece and is equal to the ratio of the absorbed power ($P_{abs}$) by the keyhole wall to the total laser power ($P$) [14]:

$$\eta_A = \frac{P_{abs}}{P} \quad (5)$$

It is worth noting that not all the absorbed laser power will be consumed for the melting but part of it will be lost by heat conduction through the BM. The thermal efficiency ($\eta_{th}$) is defined as the portion of the absorbed laser power that produced the weld seam and is equal to the ratio of the heat of melting ($P_{melting}$) divided by the absorbed laser power ($P_{abs}$):

$$\eta_{th} = \frac{P_{melting}}{P_{abs}} \quad (6)$$

The laser process efficiency ($\eta_P$) according to Dausinger et al. [14] can be calculated as:

$$\eta_P = \eta_A \eta_{th} \quad (7)$$

By substituting Eqs. (5) and (6) into Eq. (7), the laser process efficiency ($\eta_P$) can be defined as the ratio of the melting power

Table 1
Key experiments and effective parameters for 2 and 6 mm laser welded plates

| Sample # | Thickness (mm) | Gap size (mm) | Laser power (kW) | Welding speed (m min$^{-1}$) | Wire feeding rate (m min$^{-1}$) | Defocusing (mm) | Welding type |
|---|---|---|---|---|---|---|---|
| Effect of welding speed on weld geometry | | | | | | | |
| 1 | 2 | 0.4 | 4 | 4 | 2 | 0 | Butt joint (filler wire) |
| 2 | 2 | 0.4 | 4 | 5 | 2.5 | 0 | Butt joint (filler wire) |
| 3 | 2 | 0.4 | 4 | 6 | 3 | 0 | Butt joint (filler wire) |
| 4 | 2 | 0.4 | 4 | 7 | 3.5 | 0 | Butt joint (filler wire) |
| Effect of gap size on weld geometry | | | | | | | |
| 5 | 2 | 0.1 | 4 | 6 | 0.75 | 0 | Butt joint (filler wire) |
| 6 | 2 | 0.2 | 4 | 6 | 1.4 | 0 | Butt joint (filler wire) |
| 7 | 2 | 0.3 | 4 | 6 | 2.1 | 0 | Butt joint (filler wire) |
| 8 | 2 | 0.4 | 4 | 6 | 3 | 0 | Butt joint (filler wire) |
| 9 | 2 | 0.5 | 4 | 6 | 3.5 | 0 | Butt joint (filler wire) |
| 10 | 2 | 0.6 | 4 | 6 | 4.2 | 0 | Butt joint (filler wire) |
| Effect of laser power on weld geometry | | | | | | | |
| 11 | 2 | 0.4 | 2.5 | 6 | 3 | 0 | Butt joint (filler wire) |
| 12 | 2 | 0.4 | 2.75 | 6 | 3 | 0 | Butt joint (filler wire) |
| 13 | 2 | 0.4 | 3 | 6 | 3 | 0 | Butt joint (filler wire) |
| 14 | 2 | 0.4 | 3.5 | 6 | 3 | 0 | Butt joint (filler wire) |
| 15 | 2 | 0.4 | 3.75 | 6 | 3 | 0 | Butt joint (filler wire) |
| 16 | 2 | 0.4 | 4 | 6 | 3 | 0 | Butt joint (filler wire) |
| Laser welding of 6 mm plates | | | | | | | |
| 25 | 6 | – | 4 | 5 | – | 0 | Bead on plate |
| 26 | 6 | – | 4 | 5 | – | −2 | Bead on plate |
| 27 | 6 | – | 4 | 5 | – | −4 | Bead on plate |
| 28 | 6 | 0 | 4 | 5 | 0 | −4 | Butt joint (autogenous) |
| 29 | 6 | 0 | 4 | 3 | 0 | −4 | Butt joint (autogenous) |
| 30 | 6 | 0.2 | 4 | 3 | 2 | −4 | Butt joint (filler wire) |
| 31 | 6 | 0.2 | 4 | 2 | 1.35 | −4 | Butt joint (filler wire) |
| 32 | 6 | 0.4 | 4 | 3 | 4 | −4 | Butt joint (filler wire) |
| 33 | 6 | 0.4 | 4 | 2 | 2.7 | −4 | Butt joint (filler wire) |

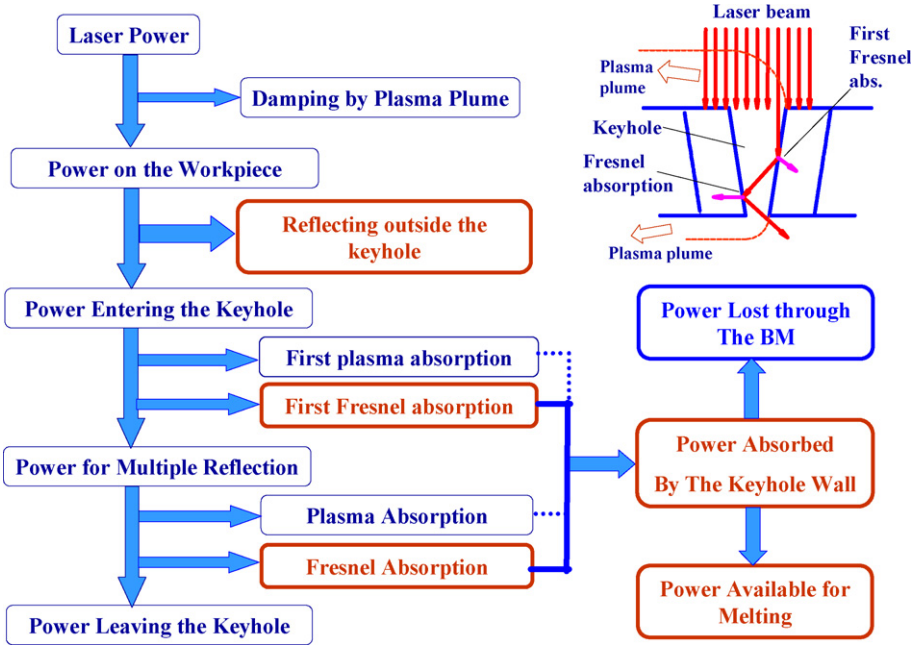


Fig. 3. Schematic diagram showing different power sources and losses during keyhole laser welding (based on the concepts presented in Refs. [9,12]).

to the total laser power:

$$\eta_P = \frac{P_{\text{melting}}}{P} \tag{8}$$

The melting ratio (MR) has been defined as the fraction of total incident laser power that is used to melt the weld metal [8,15]:

$$\text{MR} = \frac{VA_{\text{w}}\rho(C_{\text{p}}(T_{\text{mp}} - T_{\text{o}}) + \Delta H_{\text{f}})}{P} \tag{9}$$

where $A_{\text{w}}$ is the melted area (i.e. FZ area), $\rho$ density of the molten metal, $C_{\text{p}}$ specific heat, $\Delta H_{\text{f}}$ latent heat of fusion, $V$ welding speed, $T_{\text{mp}}$ melting point temperature, $T_{\text{o}}$ room temperature and $P$ incident laser power. Since the numerator represents the power required to melt the FZ metal, MR corresponds in reality to the laser process efficiency ($\eta_p$).

### 3.2. Laser coupling efficiency

To calculate the coupling efficiency ($\eta_A$), the absorbed laser power by the keyhole must be estimated from the given FZ geometry. Rosenthal [16] derived the temperature distribution in the work-piece induced by a moving line heat source:

$$T(r, \varphi) = T_{\text{o}} + \frac{P'}{2\pi k} K_{\text{o}}(Pe) \exp(-Pe\ \cos(\varphi)) \tag{10}$$

Where $P'$ is the line source strength (W m$^{-1}$), $T_0$ starting temperature, $K_o$ the modified Bessel function of second kind and zero order, $Pe$ the Peclet number which can be defined by Eq. (11) where $V$ is welding speed, and $k_{\text{d}}$ thermal diffusivity (m$^2$ s$^{-1}$) [9,10].

$$Pe\ (\text{Peclet number}) = \frac{\text{Converction heat}}{\text{Conduction heat}} = \frac{rV}{2k_{\text{d}}} \tag{11}$$

The thermal diffusivity is equal to the ratio of thermal conductivity to the product of heat capacity ($C_{\text{p}}$) and density of molten metal ($\rho$):

$$k_{\text{d}} = \frac{k}{\rho C_{\text{p}}} \tag{12}$$

In Eq. (10), the polar coordinates ($r$ and $\varphi$) are measured from the beam axis, which is assumed to be in the center of a conical keyhole shape [10] as illustrated in Fig. 4. For a given FZ geometry the average line source strength can be calculated from Eq. (10), by applying the boundary condition at the partial melted zone (PMZ) where $T$ is equal to $T_{\text{mp}}$, $r$ is half the average width of the FZ and $\varphi$ is $\pm\pi/2$. After calculating the average line source strength, the power absorbed by the keyhole ($P_{\text{abs}}$) can be calculated by multiplying the average line source strength ($P'_{\text{average}}$) by the penetration depth (Pd) [10]:

$$P_{\text{abs}} = P'_{\text{average}}\text{Pd} \tag{13}$$

### 3.3. Efficiencies calculation

The calculated coupling, thermal and process efficiencies for samples 29 and 30 are shown in Table 2. The physical properties for pure Mg at melting point (Table 3) were used for this purpose because the accurate physical properties of the ZE41A-T5 alloy at liquid state are not available except for its melting temperature. Table 2 shows that applying filler wire (sample 30) resulted in a reduction in the coupling efficiency by 12% and an increase in thermal efficiency by 8% compared with the autogenous welding (sample 29). The decrease in coupling efficiency is probably due to the reflection of laser rays outside the keyhole. This method of efficiency calculation will be combined into the model used in this work. The efficiency values obtained from both the simulated and experimental weld geometries will be compared.

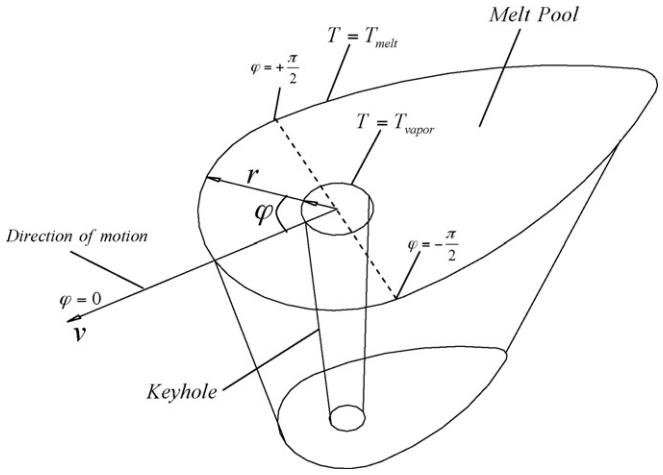


Fig. 4. Polar coordinate used at the center of the keyhole.

## 4. Modeling of keyhole-mode laser welding

The objective of this section is to simulate the keyhole and fusion zone generated during the keyhole-mode laser welding through combining various models and concepts. The model will help to better understand the laser welding process and the effect of different process parameters on the keyhole and fusion zone profiles. Also the model can reduce the time necessary to find the suitable parameters to produce fully penetrated weld joints. In this model, the following assumptions were implemented:

- The keyhole profile is symmetrical in the plane perpendicular to the welding direction.
- The laser heat source is assumed to be a line-heating source acting along the center of the keyhole.
- The equation describing the energy balance between the heat loss at the keyhole wall and the absorbed intensity by the plasma was solved in the plane perpendicular to welding direction. The selection of this plane allows the calculation of the melting temperature isothermal profile.
- A Gaussian-like distribution was assumed for the intensity of the laser beam [9,10].
- Reflection of the laser ray from the keyhole wall follows the Fresnel formulation which assumes that the angle of incidence is equal to the angle of reflection [12].

Table 2
Calculated laser efficiencies for samples 29 and 30

| Sample # | Process type | Coupling efficiency (% $P_{abs}/P_{total}$) | Thermal efficiency (% $P_{melting}/P_{abs}$) | Process (melting) efficiency (% $P_{melting}/P_{abs}$) |
|---|---|---|---|---|
| 29 | (Autogenous) | 70.4 | 35.1 | 24.7 |
| 30 | (Applying filler wire) | 58.3 | 43.3 | 25.2 |

Table 3
Physical Properties for Pure Mg, ZE41A and Pure Al

| Properties | Pure Mg | | ZE41 | | Pure Al | |
|---|---|---|---|---|---|---|
| Melting point (°C) | 650 | [23] | 530–640 | [24] | 660 | [23] |
| Thermal conductivity ($W\,M^{-1}\,K^{-1}$) | $78_{melting}$ | [23] | $109_{room\ T.}$ | [24] | $94_{melting}$ | [23] |
| Specific heat ($J\,Kg^{-1}\,K^{-1}$) | $1360_{melting}$ | [23] | $960_{room\ T.}$ | [24] | $1080_{melting}$ | [23] |
| Density ($Kg\,M^{-3}$) | $1590_{melting}$ | [23] | $1840_{room\ T.}$ | [24] | $2385_{melting}$ | [23] |
| Boiling point (°C) | 1110 | [1] | – | | 2520 | [23] |
| Heat of fusion ($J\,Kg^{-1}$) | $3.7 \times 10^5$ | [23] | – | | $4 \times 10^5$ | [23] |

### 4.1. Energy balance at the keyhole wall for first fresnel absorption

The heat loss from the keyhole wall depends on the absorbed laser intensity, which is described by the following equation [9]:

$$q_v = I_{ab} \tan(\theta) \tag{14}$$

Where $q_v$ is heat flow in a particular keyhole layer ($W\,m^{-2}$), $\theta$ is the angle of the keyhole at the particular layer, and $I_{ab}$ is the absorbed intensity at the keyhole wall. This intensity is equal to the local intensity available at the layer multiplied by the Fresnel absorption coefficient as will be described later. Fig. 5 is a graphical illustration of these terms.

### 4.2. Heat flow equation at the keyhole wall

The heat absorbed by the keyhole wall is equal to the heat loss through the keyhole [9]. The heat flow was determined by applying Fourier's law of heat conduction that can be simplified as:

$$q = -k\frac{\partial T}{\partial r} \tag{15}$$

By substituting the moving line source temperature field, Eq. (10), into Eq. (15), the following heat flow equation was derived by Kaplan [9] and Lampa et al. [10]:

$$q(r,\varphi) = \frac{1}{r}(T - T_o)kPe\left(\cos\varphi + \frac{K_1(Pe)}{K_0(Pe)}\right) \tag{16}$$

where $q$ is the heat flow ($W\,m^{-2}$) and $K_1$ the modified Bessel function of second kind and first order. The polar coordinates $(r, \varphi)$ are shown in Fig. 4. As mentioned earlier, the plane of interest is perpendicular to welding direction. At the boundary between the PMZ and HAZ, $r$ is equal to ± half the average width of fusion zone, and $\varphi \pm \pi/2$.

### 4.3. Intensity distribution for the laser beam

The intensity distribution of the laser beam is assumed to follow the Gaussian-like distribution. Under these conditions, the maximum peak intensity ($I_{oo}$) is located at the focal plane at

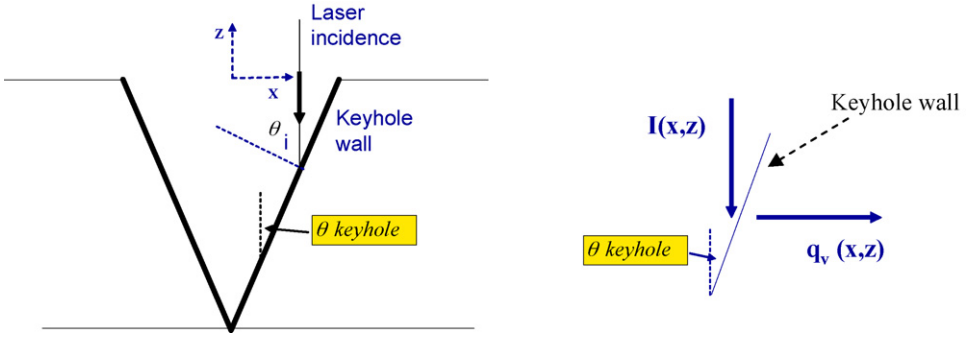


Fig. 5. Energy balance for first fresnel absorption [9].

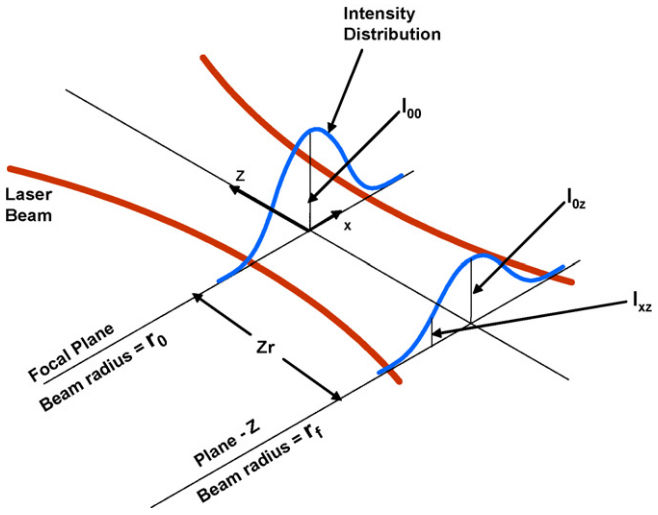


Fig. 6. Intensity distribution for the laser beam [17].

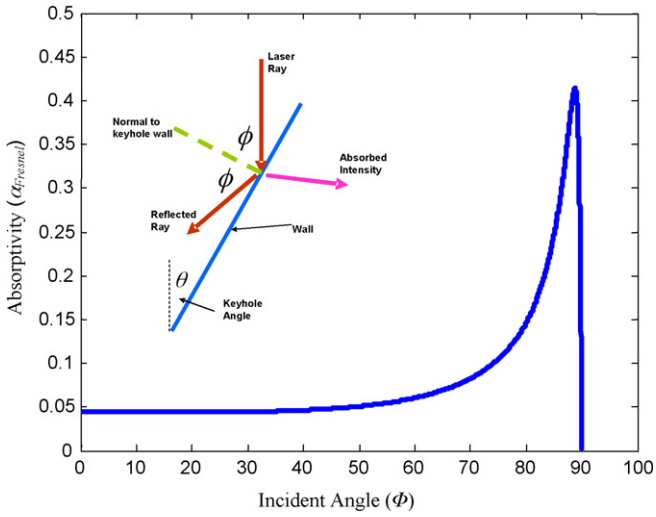


Fig. 7. Calculated absorptivity of Al to Nd:YAG laser beam at different incident angles at room temperature.

zero radius, and the intensity decreases as the laser beam moves away from the focal point in $x$ and $z$ directions as shown in Fig. 6. The intensity of the laser beam at any point can be calculated by the following equation [9,10,17]:

$$I(x, z) = I_{oz}\ \exp(-2x^2/r_f^2) \tag{17}$$

Where $I_{oz}$ is the peak intensity at any $z$-plane and $r_f$ is the beam radius at any $z$-plane and can be calculated by the following equations [9,17]:

$$I_{oz} = I_{oo}\left(\frac{r_o}{r_f}\right)^2 \tag{18}$$

and,

$$r_f = r_o\left[1 + \left(\frac{z - z_0}{z_r}\right)^2\right]^{1/2} \tag{19}$$

Where $Z_0$ is the defocusing distance (i.e the position of the focal plane relative to the plate top surface), and $Z_r$ is the Rayleigh length where the peak intensity at $Z_r$-plane is equal to half the maximum intensity at the focal plane ($I_{oo}$). Rayleigh length can be calculated by the following equation [9]:

$$Z_r = \pm 2r_o(f - \text{number}) \tag{20}$$

Where $f$-number is defined as the ratio of a lens focal length to the diameter of its entrance pupil. In the present investigation, the Rayleigh length for the lens used was measured to be about 2.33 mm.

The maximum intensity can be computed using the following equation [9,17]:

$$I_{oo} = \frac{2P}{r_o^2\pi} \tag{21}$$

Where $P$ is the laser power and $r_o$ the beam focal radius.

### 4.4. Calculation of the fresnel absorption coefficient

The laser ray will experience reflection and absorption by the keyhole wall. At the liquid–vapor interface the angle of incidence of the laser beam is assumed to be equal to the angle of reflection. The absorption coefficient of the laser ray ($\alpha_{Fresnel}$) can be calculated using Fresnel formula for circular or random polarized light as follows [12,18,19]:

$$\alpha_{Fresnel} = 1 - \frac{1}{2}\left(\frac{1 + (1 - \varepsilon\ \cos\phi)^2}{1 + (1 + \varepsilon\ \cos\phi)^2} + \frac{\varepsilon^2 - 2\varepsilon\ \cos\phi + 2\cos^2\phi}{\varepsilon^2 + 2\varepsilon\ \cos\phi + 2\cos^2\phi}\right) \tag{22}$$

Where $\phi$ is the angle of incidence (Fig. 7), and $\varepsilon$ is a material-dependant constant. The absorptivity of Mg at perpendicular incidence for Nd:YAG laser is unknown. Therefore, a value for Al element (i.e. 4%) at 1.06 μm wavelength was used [14]. The value of $\varepsilon$ was estimated by substituting ($\phi = 0$, $\alpha_{Fresnel}^{perpendicular} = 0.04$) in Eq. (22) and found to be 0.03.

The absorbed intensity can be calculated by the following equation:

$$I_{ab} = I(x, y)\alpha_{Fresnel} \tag{23}$$

### 4.5. Plasma absorption

The plasma absorption appearing in the keyhole-mode laser welding affects the characteristics of the keyhole by producing a wider and less penetrated keyhole [12]. The absorbed intensity in the keyhole by the inverse Bremsstrahlung action will be deposited back to the keyhole wall by radiation [20]. The absorbed intensity by plasma can be calculated by the following equation [9,12]:

$$I_{Plasma} = I_{incident}(1 - \exp(-\alpha_{IB}L)) \tag{24}$$

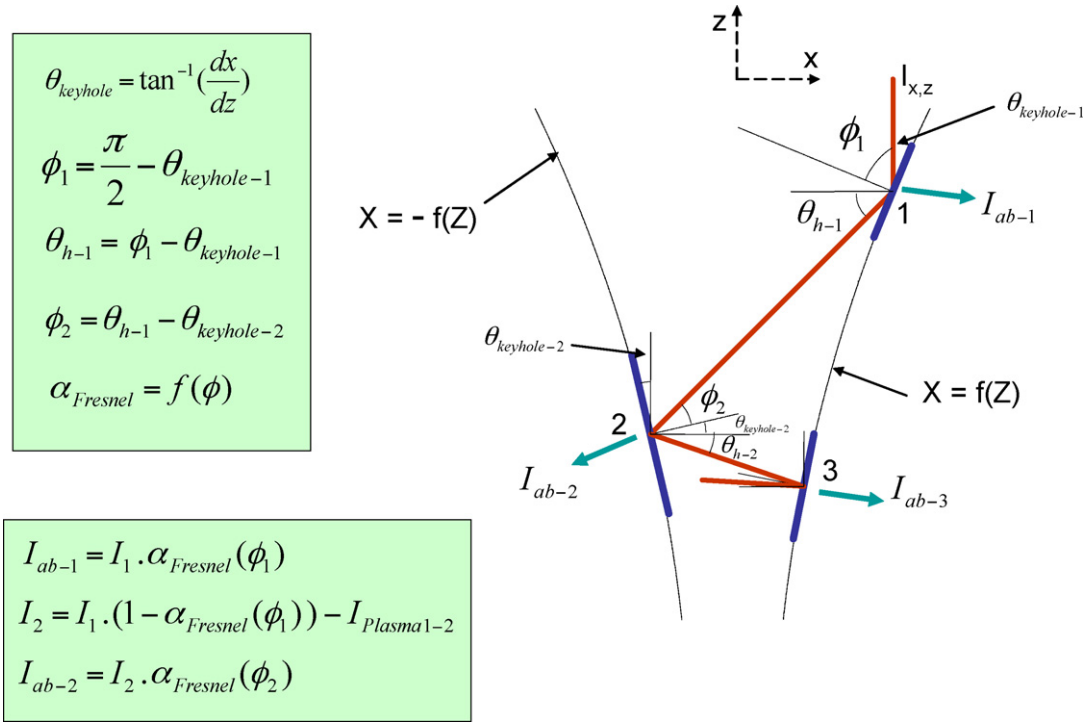


Fig. 8. Geometrical analysis for multiple reflections inside the keyhole.

Where $L$ is the path length of the ray inside the plasma, and $\alpha_{IB}$ is the inverse Bremsstrahlung coefficient, which is a function of the density of electrons, degree of ionization and temperature in the keyhole. It has been reported that, $\alpha_{IB}$ ranges from 100 to 200 $m^{-1}$ [9,12]. In the present work an average value of 150 $m^{-1}$ was used. The plasma absorption coefficient $(1 - \exp(-\alpha_{IB}L))$ is proportional to the square of the wavelength [18]. Since the wavelength for $CO_2$ laser is 10.6 and 1.06 μm for Nd:YAG, the plasma absorption in Nd:YAG laser is 1% of the plasma absorption in $CO_2$ laser. Kaplan [9] reported that the plasma plume absorption outside the keyhole is approximately 1% of the incident laser power for $CO_2$ lasers. Therefore, the plasma plume (outside the keyhole) was neglected here because of the short wavelength of the Nd:YAG laser, whereas the plasma absorption between the multiple reflections inside the keyhole was calculated.

### 4.6. Multiple reflections of the laser beam

After calculating the keyhole profile by considering only the first Fresnel absorption, the keyhole profile was converted to polynomial equation using the least squares method in order to calculate the slope and the Fresnel absorption coefficient at any location. Between two reflections the laser beam loses intensity because of the plasma absorption as mentioned above. The geometrical and intensity calculation between the two reflections is illustrated in Fig. 8. In Kaplan's analysis [9], the energy balance equation reflects the effect of all mechanisms (first Fresnel, multiple reflections, plasma), but the effect of multiple reflection was assumed to be acting only in the horizontal direction since the angle between the multiple reflected ray and keyhole wall is assumed to be always 90°. Since this is not the typical case in the multiple reflections, Kaplan's equation has been modified in this work as shown in Eq. (25). The absorbed intensity from multiple reflections will add to the direct Fresnel intensity to produce the total absorbed intensity in the particular layer whereas the plasma absorption will aid in widening the keyhole [11,12].

$$\tan(\theta_{\text{keyhole}}^{\text{layer}}) = \frac{q^{\text{layer}} - I_{\text{plasma}}^{\text{layer}}}{I_{\text{Fr1}}^{\text{layer}} + I_{\text{Fr-Mr}}^{\text{layer}}} \quad (25)$$

Where the subscripts Fr and Mr denote Fresnel and multiple reflections, respectively.

### 4.7. Computer simulation of the keyhole laser welding process

MATLAB software was used to simulate the keyhole laser welding process as shown in Fig. 9. The procedure used for this purpose is:

**Stage 1**: To calculate the keyhole profile by considering only the energy balance between the first Fresnel absorption and the heat loss at the keyhole wall. The calculation starts from the plate top surface and continues downward to solve Eq. (14) layer by layer. The layer thickness is variable and taken as 10 μm in this simulation. The first layer will determine the keyhole top radius by assuming a starting angle of 45° [9,10]. This angle will determine the radius of the second layer at which the heat loss and absorbed intensity will

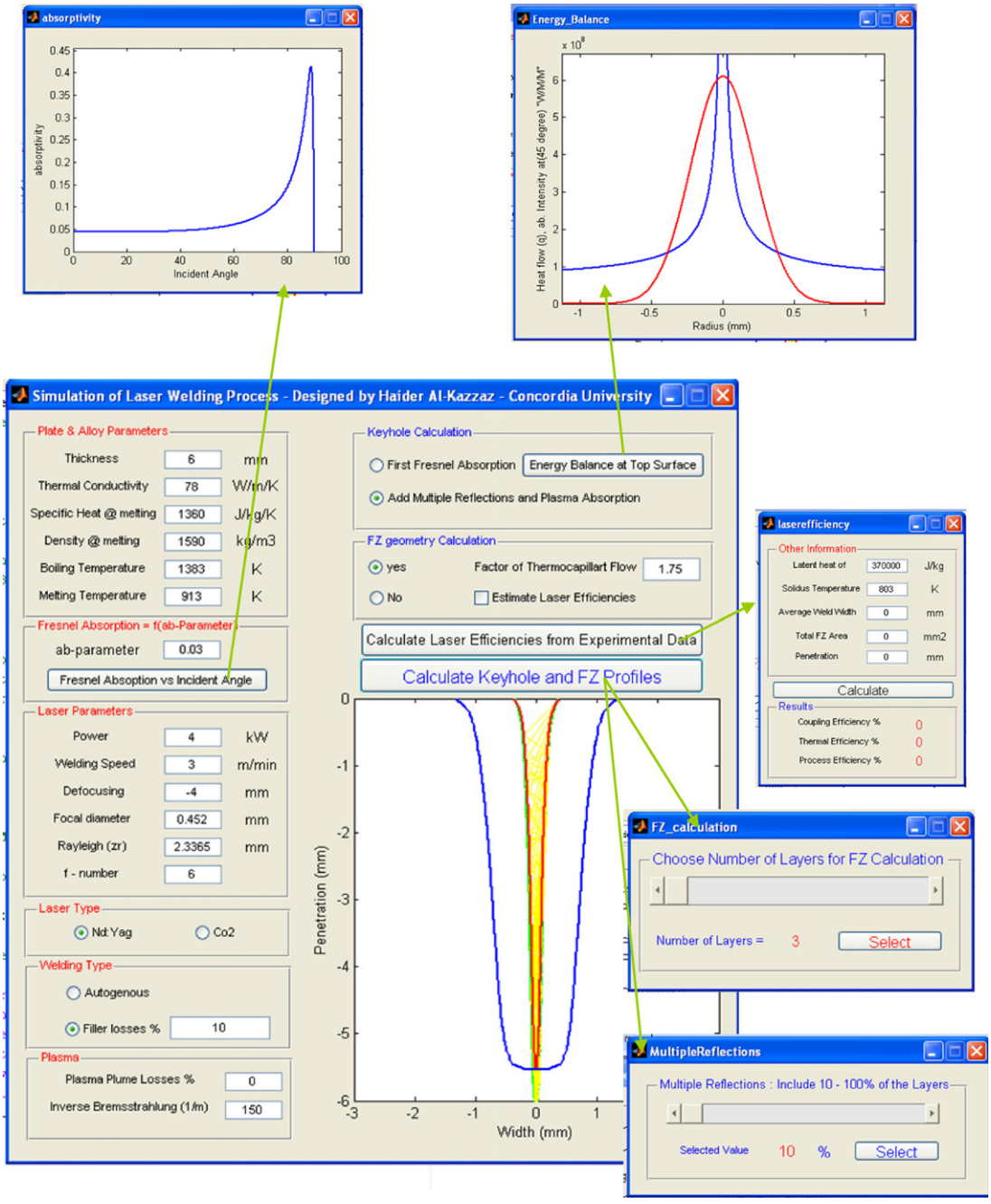


Fig. 9. Graphical user interface for the laser welding simulation program.

be calculated and the only unknown is the keyhole angle. At each layer the Fresnel absorption coefficient and the heat loss will be calculated to determine the keyhole angle for that step. The calculation will be completed when the keyhole radius reaches zero (for the blind keyhole) or when the penetration depth is equal to the plate thickness (for the open keyhole mode).

**Stage 2**: Using the keyhole profile obtained from Stage 1, the multiple reflections and plasma absorption occurring during the process are calculated during this stage. Each absorption was registered to a corresponding layer to enable the calculation of the keyhole profile for the next iteration. This was achieved by converting the keyhole profile into polynomial equation using curve fitting technique. With such an approach, it was possible to calculate the intersection of each multiple reflection, ray path, keyhole angle, and Fresnel and plasma absorptions.

**Stage 3**: To recalculate the keyhole profile by considering all the mechanisms as described in Eq. (25). The use of filler wire caused a reduction in the coupling efficiency by 10–14% (Table 2). Therefore, a value of 10% was considered to be the losses of laser power and inten-

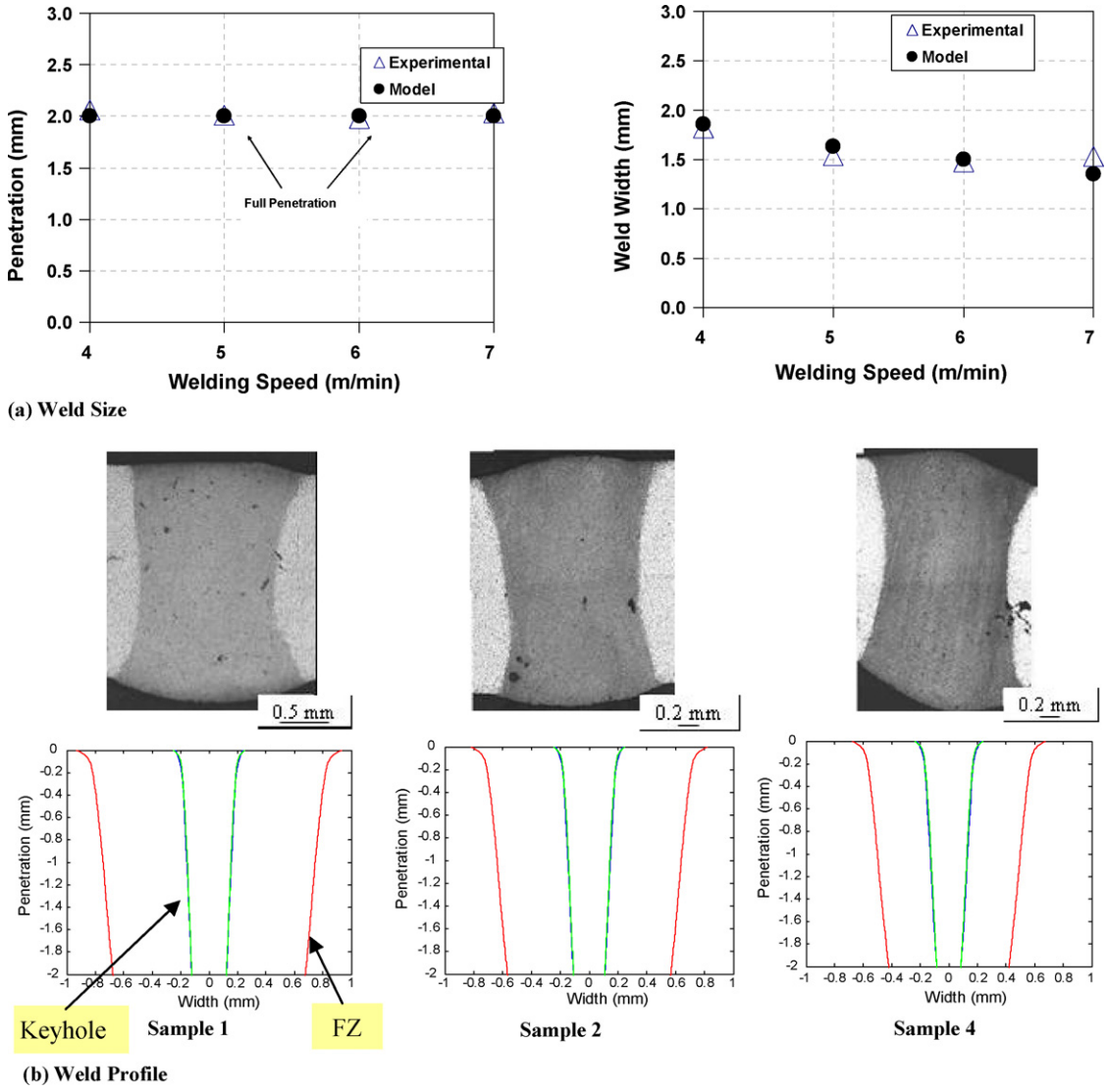


Fig. 10. Comparison between (a) experimental and (b) calculated weld geometry for laser welding of 2 mm plates at variable welding speeds.

sity before entering the keyhole. The source strength at each layer will be calculated using Eq. (10) by taking the boundary condition at the keyhole wall as: $r = r_{keyhole}$, $T = T_v$, and $\varphi = \pm\pi/2$.

**Stage 4**: To calculate the FZ geometry. Eq. (10) was used to determine the radius of the melting isotherm at each layer since the source strength for each layer was calculated in the previous stage. Therefore, the FZ radius can be calculated for each layer by applying the boundary condition at the PMZ (i.e. $T = T_{mp}$, $r$ = half width of the fusion zone, $\varphi = \pm\pi/2$). Sample 29 was used to estimate the effect of thermocapillary flow on the FZ top width. It was found that a correction factor with a magnitude of 1.75 was sufficient to compensate source strength at each layer in this work.

The program developed in this study was also used to calculate laser efficiencies as discussed in Section 3.

## 5. Results and discussion

Fig. 10 compares the effect of welding speed on weld geometry using both the modeling and the experimental results. The penetration depth and top bead width for both modeling and experimental results are in good agreement. It was found that weld width and fusion zone area decrease with increasing welding speed. Also, it can be seen in this figure that the 2-mm laser welded joints exhibited larger width at the top and the root due to the effect of thermocapillary flow in these locations. The Marangoni (thermocapillary) flow is induced by the surface tension gradient and the friction force between the vapor jet and the molten metal, causing the widening of weld geometry at both the top and the bottom in open keyhole condition [10,21]. The hourglass weld shape with wide weld profile at the root proved that the keyhole was open at the root, which is consistent with the simulated keyhole profile as shown in Fig. 10–b. The discrepancies in the weld profiles between the model and the

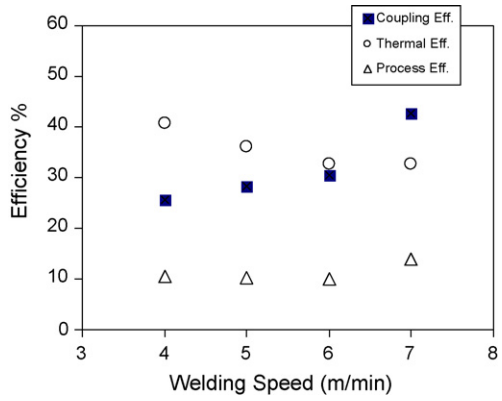


Fig. 11. Effect of welding speed on coupling, thermal and process efficiencies.

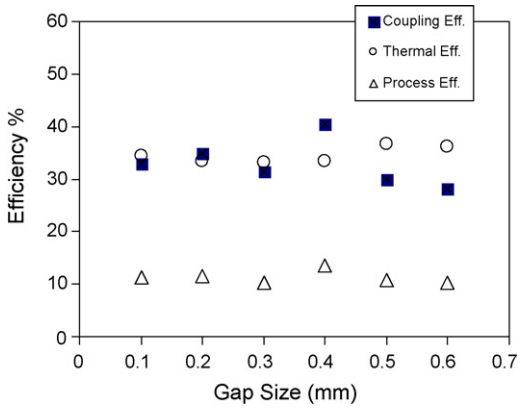


Fig. 13. Effect of gap size on coupling, thermal and process efficiencies.

experiments are probably due to the thermocapillary flow inside the weld pool which was not included in this model.

Fig. 11 shows the effect of welding speed on the coupling, thermal and process efficiencies. As the welding speed increased from 4 to 7 m min$^{-1}$, the coupling efficiency increased from 25 to 42%. The effect of welding speed on the average keyhole angle was simulated as shown in Fig. 12. The keyhole angle with $y$-axis was increased from 3.9° to 4.5° as the welding speed increased from 4 to 6 m min$^{-1}$, causing the increase in the number of multiple reflections (Fig. 12). Thus the coupling efficiency was improved at higher welding speed. This increase in welding speed also decreased the root keyhole width (Figs. 10 and 12). Fig. 11 also shows that the thermal efficiency dropped with increasing welding speed. This reduction in thermal efficiency balanced the increase in the coupling efficiency, resulting in an approximately constant melting or process efficiency. The simulation for sample 4 welded at 7 m min$^{-1}$ shows that the keyhole was open at the root (Fig. 10) but the slight increase in process efficiency (Fig. 11) can be attributed to the large misalignment of the workpieces.

The effect of gap size on the efficiencies is shown in Fig. 13. With increasing gap sizes from 0.1 to 0.6 mm, the corresponding increase in filler wire feed rate did not cause any significant change in the process efficiency indicating that the reflection losses due to the interaction of the laser beam with filler wire were almost constant for different feed rates. The coupling efficiency was at maximum value at 0.4 mm gap size, which seems to be a suitable size for molten flow and formation of the keyhole.

The effect of laser power on weld geometry and the comparison between the modeling and the experimental results are shown in Fig. 14. Both the modeled and experimental sections show that the keyhole varied from the closed (blind) to the open profile at root and the FZ geometry changed from the partial to the full penetration when the laser power increased from 2.5 to 4 kW.

Fig. 15 shows the effect of laser power on the coupling, thermal and process efficiencies. Increasing the laser power leads to increase in fusion area due to the increase in the coupling efficiency, but as indicated in Fig. 15 there was a drop in the coupling efficiency at laser powers between 3 and 3.75 kW. This drop in coupling efficiency is probably due to the change from the partially penetrated blind keyhole to fully penetrated open keyhole, which ultimately results in the loss of laser intensity at the keyhole root. Further increase in laser power (here above 3.75 kW) will surpass the loss of laser intensity at the root, causing an increase in the coupling efficiency due to insignificant variations in the root size at higher laser powers. This variation in coupling efficiency of laser welding process and the corresponding variation in weld geometry during the change from the partial to full penetration passing through the transitional

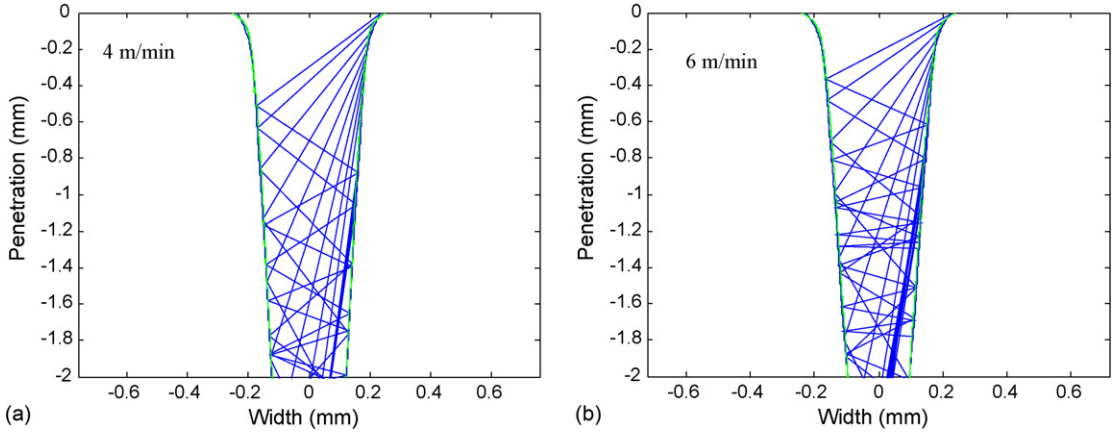


Fig. 12. The Effect of welding speed on the keyhole shape and the multiple reflections (a) 4 and (b) 6 m min$^{-1}$.

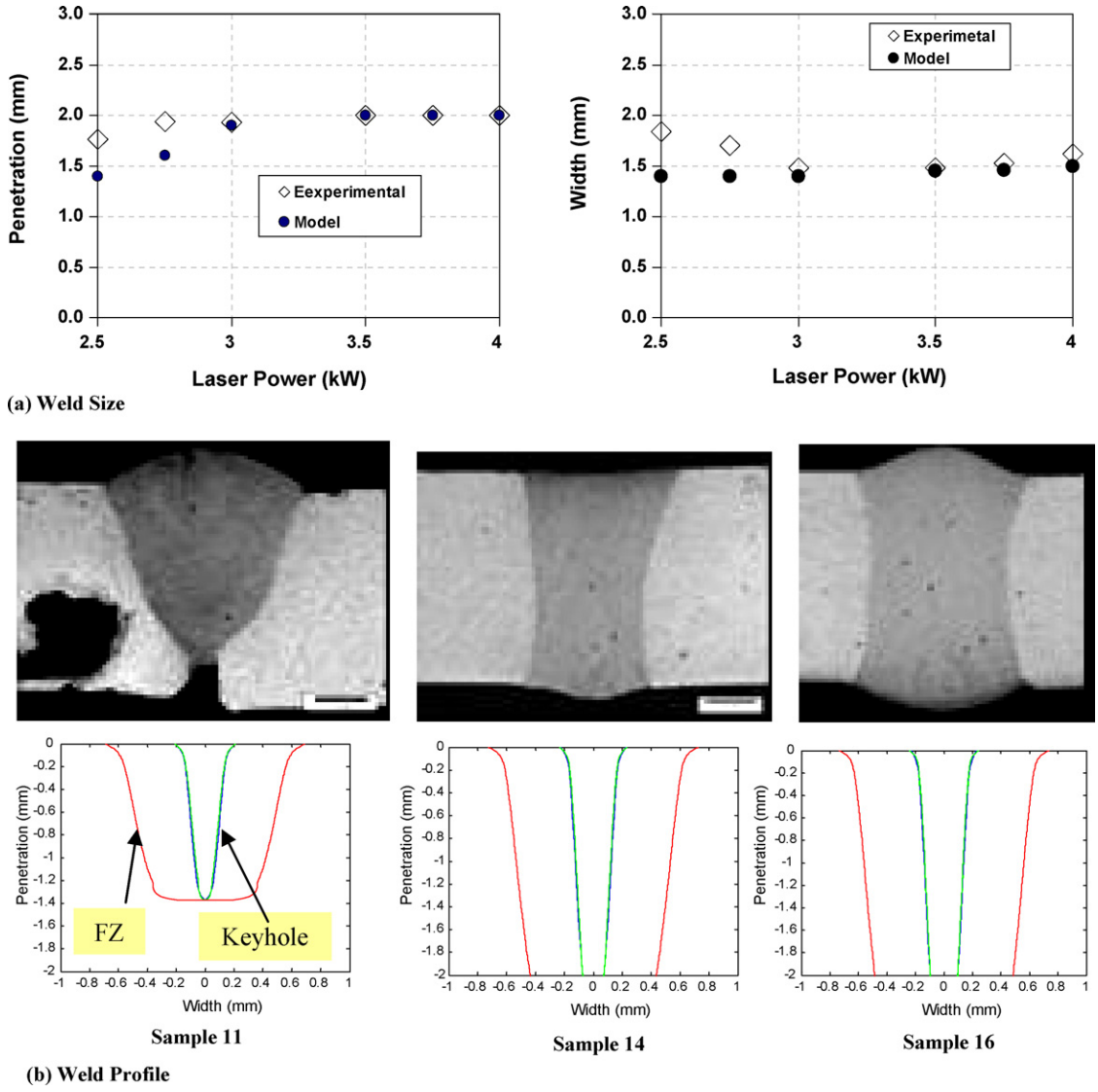


Fig. 14. Comparison between experimental and calculated weld geometry for laser welding of 2 mm plates at variable laser power (a) weld size (b) weld.

region from the blind to the open keyhole was also reported by Krasnoperov et al. [21].

For the bead-on-plate laser welding (Fig. 16), both the experimental and modeling results indicate that the penetration depth increased slightly as the defocusing varied from 0 to −2 mm. However, a further increase in defocusing distance (−4 mm) caused a reduction in penetration depth compared with defocusing at −2 mm. Also as indicated above, the maximum intensity of the laser beam is located at the focal point, and the peak intensity decreases as moving below or above the focal point. The effective intensities of the laser beam are located within ± Rayleigh length (in this setup this value is equal to 2.34 mm); at a distance equal to ± one Rayleigh length from the focal plane, the peak intensity drops to one half the peak intensity [17]. When the defocusing distance varied from 0 to −2 mm, the effective intensities were located inside the material (plate), which increased the coupling efficiency between the laser beam and the plate, but at the same time the laser intensity available on the top surface was reduced because of the increase in laser beam diameter. The discrepancies observed between the modeling and the experimental results especially for sample 26 are probably due to the variations in the surface condition or physical properties between pure Mg and ZE41A-T5 alloy. Further increase

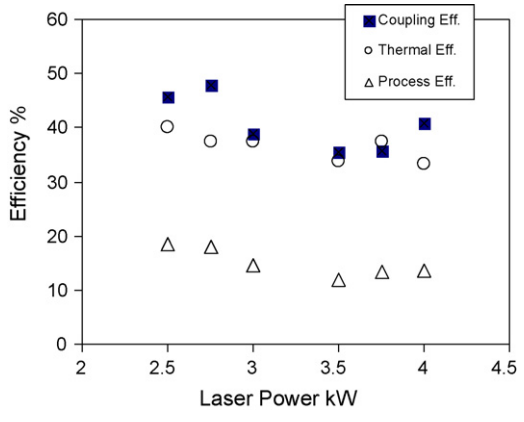


Fig. 15. Effect of laser power on coupling, thermal and process efficiencies.

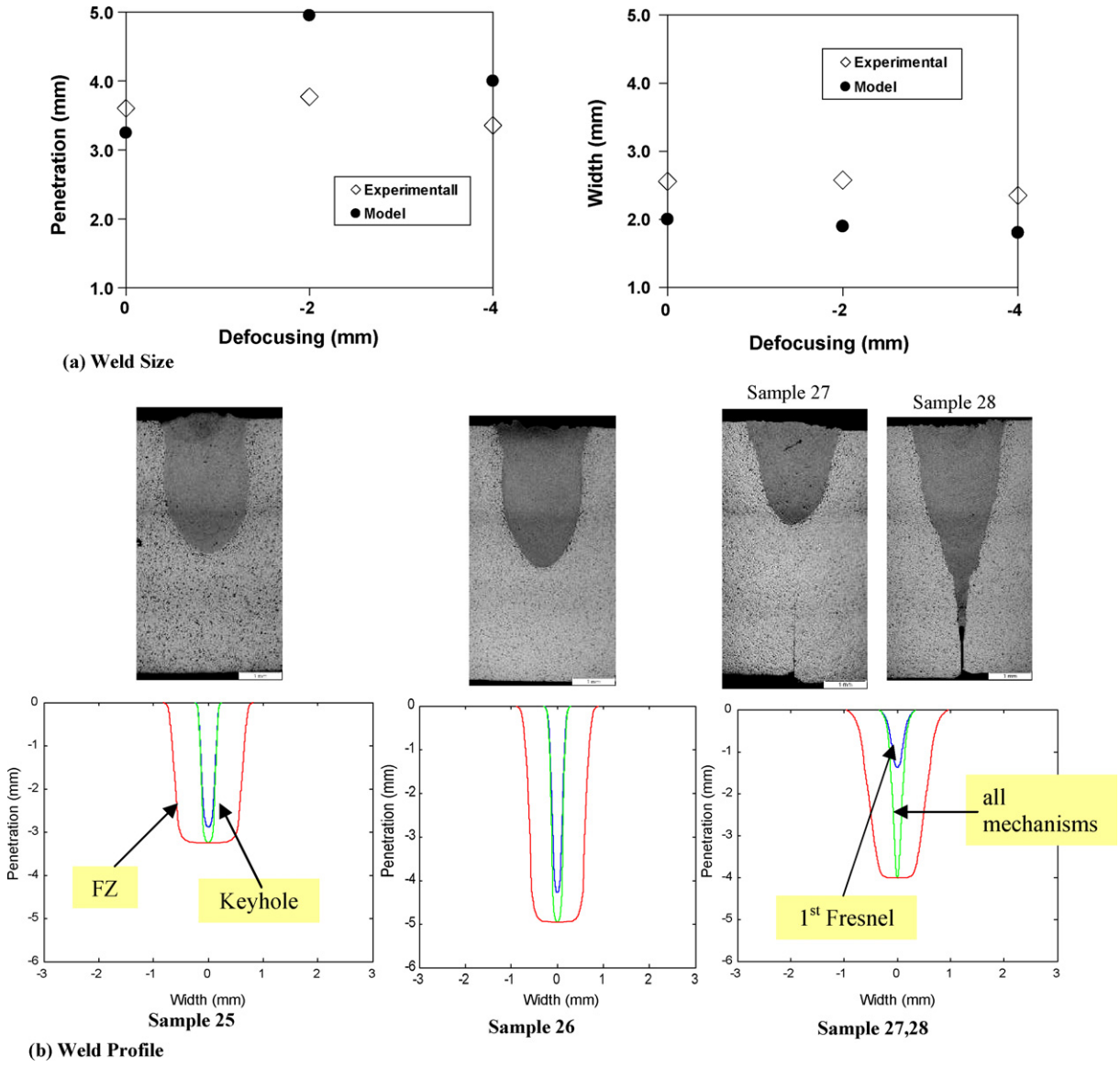


Fig. 16. Comparison between the experimental results and the model for 6 mm bead-on-plate laser welding (a) weld size (b) weld profile.

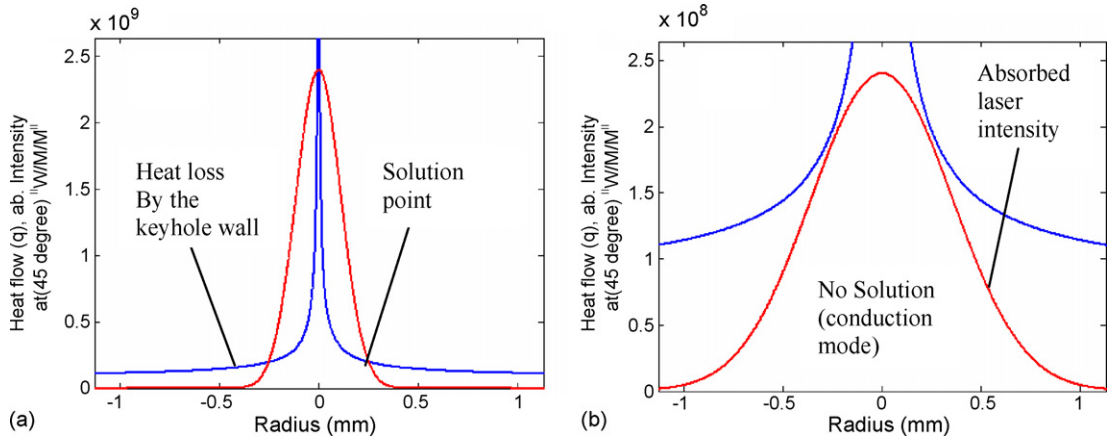


Fig. 17. Energy balance between the heat loss and the absorbed intensity at the keyhole top opening showing the effect of defocusing on keyhole formation: (a) surface defocusing, (b) at −7 mm defocusing.

in defocusing distance to −4 mm decreases laser power density around or below the threshold value required to produce the keyhole [14,17]. Therefore, the laser welding process changed from the keyhole mode (samples 25 and 26) to the conduction mode (sample 27) since the aspect ratio (penetration depth/top width) for keyhole mode should usually be greater than 1.2 [22]. Both samples 27 (bead-on-plate) and 28 (butt joint at zero gap) had the same laser welding parameters. Sample 27 exhibited a conduction or shallow keyhole penetration whereas sample 28 showed a deeper keyhole mode welding. Thus, the power density used for samples 27 and 28 is around the threshold value, i.e. $6.45 \times 10^5$ W cm$^{-2}$. The obtained results for samples 27 and 28 also indicate that the welding mode significantly influences the penetration depth values obtained with and without multiple reflections. Fig. 17 illustrates the effect of defocusing on the keyhole formation and top keyhole radius obtained by solving the energy balance between the absorbed laser intensity and the heat lost through the keyhole wall. Furthermore, Fig. 17b shows that the excessive increase in defocusing (e.g. −7 mm) leads to a conduction mode since there is no balance between the heat lost and the absorbed intensity. In other words, the applied intensity at the top plate surface is not high enough to form a keyhole.

Fig. 18 shows a comparison between the modeling and experimental results for laser welding of 6-mm thick sheets. The experimental results for fully penetrated 6-mm plates shows a widening in the lower half sections of the weld profiles due to multiple reflections and plasma absorption. Multiple reflections were highly concentrated in the lower part of the keyhole as simulated for samples 30 and 32 in Fig. 18. This increase in multiple reflections caused an increase in plasma absorption in that region, resulting in the widening of the weld profile. The model also predicts a gradual change and widening in weld pro-

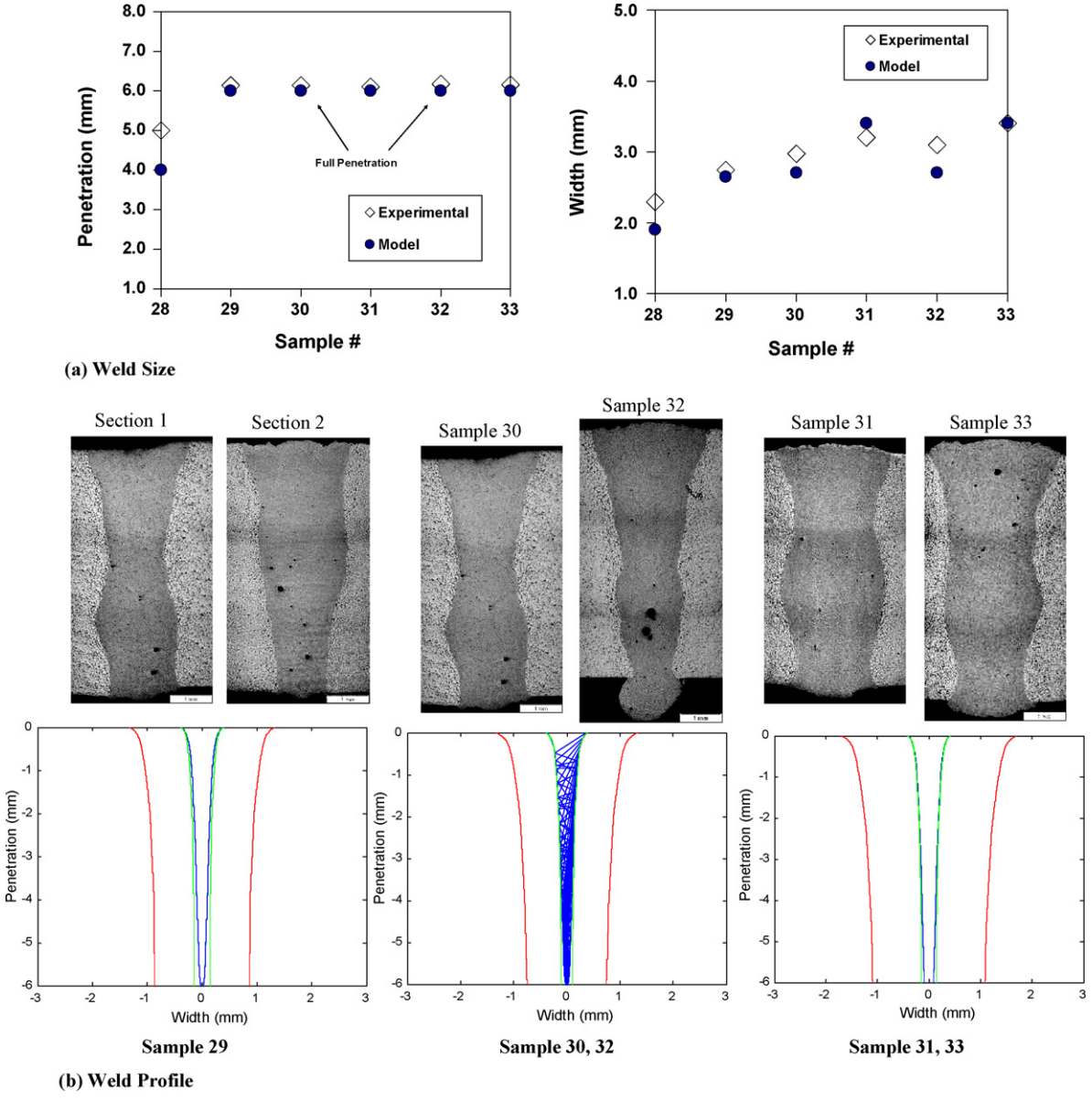


Fig. 18. Comparison between the experimental results and the model for butt joints (6 mm) laser welded plates: (a) weld size, (b) weld.

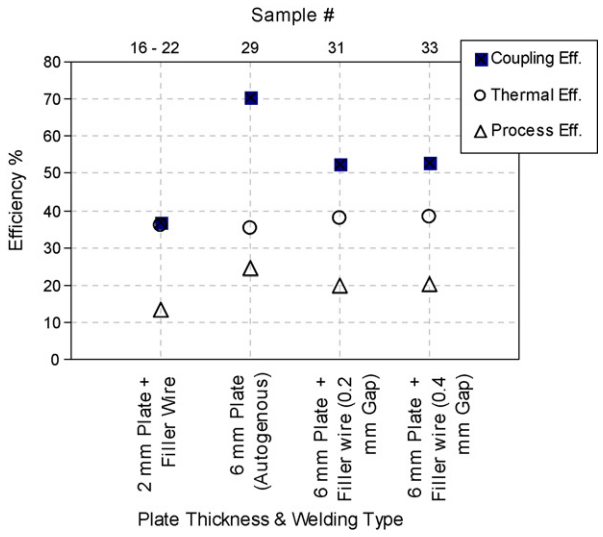


Fig. 19. Effect of penetration depth and welding type on the coupling, thermal and process efficiencies.

file mainly in the lower zone, which is in agreement with the experimental observations.

Fig. 19 shows a comparison between the coupling, thermal and melting efficiencies of the successfully welded 2 and 6 mm joints. The higher coupling efficiency was obtained for the 6 mm plates due to the multiple reflection of the laser beam inside the keyhole. Higher penetration depth will increase multiple reflection and plasma absorption inside the keyhole. Fig. 19 also shows the efficiency values for the 6 mm laser welded plates at 0.2 and 0.4 mm gap size. It can be seen that the feed rate had little influence on the variation of the coupling, thermal and process efficiency.

## 6. Summary and conclusions

The laser welding process for ZE41A-T5 Mg sand castings using 1.6 mm filler wire EZ33A-T5 was studied for 2- and 6-mm butt joints, or bead-on-plate through experimental and modeling investigations. The plates were laser welded using the following process parameters: laser power (2.5–4 kW), welding speed (4–7 m $min^{-1}$), defocusing (0 to −4 mm), and gap size (0.1–0.6 mm). The simulation of laser welding process was developed through combining and integrating various models and concepts to calculate the keyhole and weld geometry profiles. The modeled weld bead width, penetration depth and weld profile were found to be in good agreement with the experimental results. The following conclusions can be drawn:

- Weld width and fusion area decrease with increasing welding speed. In partially penetrated welding, penetration depth also decreases with increasing welding speed.
- Excessive decrease in laser power or increase in defocusing distance can decrease surface power density, leading to the change of the welding mode from fully penetrated keyhole, to partially penetrated keyhole, and then to conduction mode.
- Laser process efficiencies for 2-mm butt joints were found to be around 13%, lower than those for 6-mm joints (20–25%). The corresponding coupling efficiencies for 2-mm plates were also significantly lower than those for the 6-mm butt joints due to the lower number of multiple reflections inside the keyhole.
- No significant effect of the filler wire feed rate on the coupling and melting efficiencies was found.
- Also, the developed model can be used to calculate the instantaneous temperature gradient in the weld pool as well as in the base metal around the heat source.

## References

[1] K.G. Watkins, Laser welding of magnesium alloys, in: Magnesium Technology 2003, Proceedings of the Symposium held during the 2003 TMS Annual Meeting, San Diego, CA, United States, 2003, pp. 153–156.
[2] C. Dawes, C. Eng, Laser Welding, McGraw-Hill, Inc., USA, 1992.
[3] H. Haferkamp, F. von Alvensleben, I. Burmester, M. Niemeyer, The characteristics of laser beam welded magnesium alloys, Proceeding of the Laser Material Processing Conference, ICALEO' 97, 1997, pp. G/140–G/149.
[4] H. Zhao, T. Debroy, Pore formation during laser beam welding of die-cast magnesium alloy AM60B—mechanism and remedy, Welding J. 80 (8) (2001) 204-s–210-s.
[5] W.W. Duley, Laser Welding, John Wiley & Sons, Inc., USA, 1998.
[6] S.A. Tsirkas, P. Papanikos, Th. Kermanidis, Numerical simulation of the laser welding process in butt-joint specimens, J. Mater. Process. Technol. 134 (2003) 59–69.
[7] M. Pastor, H. Zhao, T. Debroy, Continuous wave-Nd:Yttrium-Aluminum-garnet laser welding of AM60B magnesium alloy, J. Laser Appl. 12 (3) (2000) 91–100.
[8] A. Punkari, D.C. Weckman, H.W. Kerr, Effects of magnesium content on dual beam Nd:YAG laser welding of Al–Mg alloys, J. Sci. Technol. Welding Joining 8 (4) (2003) 269–281.
[9] A. Kaplan, A model of deep penetration laser welding based on calculation of the keyhole profile, J. Phys. D: Appl. Phys. 27 (1994) 1805–1814.
[10] C. Lampa, A.F.H. Kaplan, J. Powell, C. Magnusson, An analytical thermodynamic model of laser welding, J. Phys. D: Appl. Phys. 30 (9) (1997) 1293–1299.
[11] X. Jin, L. Li, Y. Zhang, A study on fresnel absorption and reflections in the keyhole in deep penetration laser welding, J. Phys. D: Appl. Phys. 35 (2002) 2304–2310.
[12] Solana, G. Negro, A study of the effect of multiple reflections on the shape of the keyhole of the keyhole in the laser processing of materials, J. Phys. D: Appl. Phys. 30 (1997) 3216–3222.
[13] H. Al-Kazzaz, M. Medraj, X. Cao, M. Xiao, M. Jahazi, Effect of laser power and joint gap on weld quality of aerospace grade ZE41A-T5 magnesium alloy using Nd:YAG laser, Proceedings of the International Symposium on Magnesium Technology in the Global Age, COM 2006, 503–518 Montreal, Canada, October 1–4, 2006.
[14] F. Dausinger, J. Rapp, M. Beck, F. Faisst, R. Hack, Helmut Hugel, Welding of aluminum: a challenging opportunity for laser technology, J. Laser Appl. 8 (6) (1996) 285–290.
[15] D.T. Swift-Hook, A.E.F. Gick, Penetration welding with lasers, Welding J. 52 (11) (1973) 492s–499s.
[16] D. Rosenthal, The theory of moving sources of heat and its application to metal treatments, Trans. ASME 68 (1946) 848–866.
[17] H. Hügel, Strahlwerkzeug Laser, Teubner Studienbücher Maschinenbau, Stuttgart 1992, ISBN 3-519-06134-1.
[18] R. Ducharme, K. Williams, P. Kapadia, J. Dowden, B. Steen, M. Glowacki, The laser welding of thin metal sheets: an integrated keyhole and weld pool model with supporting experiments, J. Phys. D: Appl. Phys. 27 (1994) 1619–1627.
[19] J.Y. Lee, S.H. Ko, D.F. Farson, C.D. Yoo, Mechanism of keyhole formation and stability in stationary laser welding, J. Phys. D: Appl. Phys. 35 (2002) 1570–1576.
[20] Y. Zhang, L. Li, G. Zhang, Spectroscopic measurements of plasma inside the keyhole in deep penetration laser welding, J. Phys. D: Appl. Phys. 38 (2005) 703–710.

[21] M.Y. Krasnoperov, R.R.G.M. Pieters, I.M. Richardson, Weld pool geometry during keyhole laser welding of thin steel sheets, Sci. Technol. Welding Joining 9 (6) (2004) 501–506.
[22] X. Cao, M. Xiao, M. Jahazi, Y.L. Lin, Continuous wave Nd:YAG laser welding of sand-cast ZE41A-T5 magnesium sand casting: conduction or keyhole mode, Proceedings of the International Symposium on Aerospace Materials and Manufacturing: Development, Testing and Life Cycle Issues, Honoring William Wallace, 2nd, Aerospace Materials and Manufacturing: Development, Hamilton, ON, Canada, Aug. 22–25 2004, pp. 187–197.
[23] X. Cao, M. Jahazi, J.P. Immarigeon, W. Wallace, A review of laser welding techniques for magnesium alloys, J. Mater. Process. Technol. 171 (2) (2006) 188–204.
[24] Magnesium Elektron: http://www.magnesium-elektron.com/ (October 5, 2006).